

Precise phase control of large-scale inorganic perovskites via vapor-phase anion-exchange strategy

Guobiao Cen¹, Yufan Xia¹, Chuanxi Zhao^{1*}, Yong Fu¹, Yipeng An², Ye Yuan¹, Tingting Shi^{1*}, Wenjie Mai^{1*}

¹Siyuan Laboratory, Guangdong Provincial Engineering Technology Research Center of Vacuum Coating Technologies and New Energy Materials, Department of Physics, Jinan University, Guangzhou, Guangdong 510632, People's Republic of China.

²School of Physics & International United Henan Key Laboratory of Boron Chemistry and Advanced Energy Materials, Henan Normal University, Xinxiang, Henan 453007, China.

E-mail: tcxzhao@email.jnu.edu.cn, ttshi@email.jnu.edu.cn, wenjiemai@email.jnu.edu.cn

Keywords: precise control, large scale, bandgap engineering, anion-exchange, phase conversion

Anion exchange offers great flexibility and high precision in phase control, compositional engineering and optoelectronic property tuning. Different from previous successful anion exchange process in liquid solution, herein, we develop a vapor-phase anion-exchange strategy to realize the precise phase and bandgap control of large-scale inorganic perovskites by using gas injection cycle, producing some perovskites such as CsPbCl₃ which has never been reported in thin film morphology. *Ab-initio* calculations also provide the insightful mechanism to understand the impact of anion exchange on tuning the electronic properties and optimizing the structural stability. Furthermore, because of precise control of specific atomic concentrations, intriguing tunable photoluminescence is observed and photodetectors with tunable photoresponse edge from green to ultraviolet light can be realized accurately with an ultrahigh spectral resolution of 1 nm. Therefore, we offer a new, universal vapor-phase anion exchange method for inorganic perovskite with fine-tunable optoelectronic properties.

1. Introduction

Integration of photodetectors with gradient light-response offers a very promising prospect in the field of optoelectronic applications, such as spectrum imaging^[1], telecommunications^[2], multicolor detection^[3], and artificial vision^[4]. Conventional technology for fabricating color-selective sensors is usually based on complex color filter arrays^[5] or assembled individual photodetectors^[6]. However, considering the device complexity and high cost during the integration, some efficient strategies using composition engineering has been proposed. For example, Yang et al. reported compositionally graded semiconductor $\text{CdS}_x\text{Se}_{1-x}$ nanowire based single-nanowire spectrometers by thermal evaporation method, with spectral response along the length^[1b]. Dou et al. successfully reported multicolor CsPbX_3 heterojunction nanowires via solution-phase anion exchange and electron-beam lithography^[7]. Composition engineering is often used in the fabrication of photodetector to tune the optoelectronic properties^[8]. Until now, the large-scale growth of patterned semiconductor films with spatial compositional gradients is still challenging by solution method, but it needs to be solved for fabricating high-integrity optoelectronic devices.

Inorganic halide perovskites (CsPbX_3 , $X = \text{Cl, Br, I}$), as wide-band gap perovskites, are becoming the research spotlight due to their application in blue LEDs, photodetectors and multi-junction solar cells^[9]. It is fast and facile to transport anion and exchange halide ions in inorganic CsPbX_3 because of its low defect formation energy, existence of vacancies, as well as the labile nature of halide anions^[10]. Therefore fast anion-exchange reaction in liquid phase highly facilitates the composition engineering of CsPbX_3 perovskites^[11]. Additionally, anion exchange paves the way for fine-tuning the photoresponse range of perovskites, which can provide a powerful tool to realize color-selective sensors. Typical solution methods are post-synthesis procedure, which mixes perovskites with reactive anion precursors^{[12], [13]}. However, currently the exchange reaction involving inorganic perovskites has been realized successfully only in liquid solution^[11a, 14]. The solution procedure often introduces capping

ligands (such as oleic acid (OA), oleylamine (OLA)), which lead to high dynamic instability, form insulating layer on the surface and block the carrier transport^[15]. Moreover, solution method is usually employed to synthesize nanocrystals^[16] and quantum dots^[17] of inorganic perovskites in small scale. So far, large-scale fabrication of some wide-band gap inorganic perovskite films (such as CsPbCl₃) has not been reported. The most crucial challenge is ascribed to the ultralow solubility of CsCl in inert solvents (such as dimethylsulfoxide (DMSO), N,N-dimethylformamide (DMF), Figure S1). The evaporation of low-solubility solvent leaves behind large amounts of grain boundaries and causes plentiful defects and phase segregation, which inevitably hinder the charge transport. Previous studies indicate chlorine additives or precursors have an impact on morphology and surface defects but with little or no incorporation into perovskites^[11b, 18]. Alloying high molar amounts of Cl into perovskite lattice becomes extremely challenging, aiming for achieving high-efficiency wide-band gap perovskite tandems^[19]. Furthermore, the preliminary understandings about anion exchange of perovskites are reported^[20], but few investigation focused on mechanism into phase transformation based on first-principle calculations^[21], which is of fundamental importance to unveil the structure-property relationship.

Herein, vapor-phase anion exchange strategy has been employed for the first time to precisely control the phase engineering of inorganic perovskites. Our technique provides unique high-reactive chemical vapor, which skillfully avoid the drawbacks of solubility and defect. Meanwhile, vapor phase precise control method such as atomic layer deposition (ALD) has been proved to be an ideal interface engineering technique to passivate defect states, enhance stability, as well as improve charge extraction^[22]. Significantly, the proposed vapor-phase anion-exchange reaction in a chamber is proved to be a general strategy for many inorganic perovskites, where the anion-exchange rate and reaction extent can be delicately controlled. The absorption spectral resolution can be precisely controlled as low as 0.8 nm by gas injection cycles and reaction temperature. In order to unveil the insightful mechanism

further, Density Functional Theory (DFT) calculations are also used to investigate the results which are consistent with the experimental characterizations of anion-exchanged perovskite. By precisely controlling the localized anion exchange reaction, spatially resolved multicolor CsPbX₃ perovskite (X=Cl, Br, or alloy of two halides) heterojunctions with well-defined patterns were fabricated. Finally, self-powered, tunable photoresponse, highly stable PDs were fabricated, showing high sensitivity from ultraviolet to visible region (3.28×10^{12} Jones @ 405 nm), ultralow dark current (10^{-11} A), ultralow UV detection limit (2.57 nWcm^{-2}), as well as high spectral resolution.

2. Results

2.1. Anion-exchange Reaction and Optical Characterization

We adopt novel vapor-phase method for large-scale anion exchange of uniform and compact CsPbCl_xBr_{3-x} thin films, which avoids the drawbacks of solution methods. Typical chemical vapor anion-exchange process is schematically illustrated in Figure 1a. Firstly, a uniform CsPbBr₃ thin film with thickness of ~80 nm was spin-coated on FTO substrates, and they were subsequently transferred into a chamber with preset parameters (105 °C, 9 Pa). Secondly, the Cl ion would be disassociated when the precursor of TiCl₄ purged into the chamber, along with fast anion exchange reaction of Br. Thirdly, the composition and bandgap of CsXBr₃ thin films can be continuously tuned by selected area exchanges using facile shadow masks. The extent of the anion-exchange reaction can be controlled by gas injection cycle of precursor. To show the chemical composition distribution, we performed elemental analysis of anion-exchanged perovskite films by transmission electron microscopy-energy dispersive X-ray spectroscopy (TEM-EDS). Figure 1b-d shows the morphology and EDS mapping of perovskite thin films treated with 0, 20 and 50 gas injection cycles, respectively. In Figure 1b, uniform distribution of Cs, Pb and Br elements on the surface of as-fabricated CsPbBr₃ sample. After underwent 20 cycles of chemical vapor anion exchange,

Br would be partially substituted by Cl ions, which is corresponding to the mixed phase $\text{CsPbCl}_x\text{Br}_{3-x}$ (CsPbX_3 alloy), as shown in Figure 1c. Further extending gas injection cycle to 50, the mixed phase would be almost conversed to CsPbCl_3 phase with minor Br left. Similar chemical composition exchanges were also confirmed by corresponding SEM-EDS mappings (Figure S2). Furthermore, the structure evolution of CsPbBr_3 films under different gas injection cycles was characterized by ex-situ XRD patterns, as shown in Figure 1e. For the as-prepared CsPbBr_3 films, the diffraction peaks locate at 15.18° , 21.45° , 30.66° , corresponding well to (100), (110) and (200) planes of monoclinic phase of CsPbBr_3 (JCPDS#18-0364, $a=b=5.827 \text{ \AA}$, $c=5.891 \text{ \AA}$, $\alpha=\beta=90^\circ$, $\gamma=89.65^\circ$), respectively. After 10 cycles of anion exchange, all the diffraction peaks redshift toward larger angle direction. Further increasing gas injection cycle to 20, more intense redshift can be found, while the FTO diffraction peaks remain unchanged. When the gas injection cycles increase to 50, three diffraction peaks have moved to locations at 15.8° , 22.46° , and 32.0° which can be well indexed to (100), (101), and (200) facets of tetragonal phase CsPbCl_3 (JCPDS#18-0366, $a=b=5.584 \text{ \AA}$, $c=5.623 \text{ \AA}$, $\alpha=\beta=\gamma=90^\circ$). Here, we concentrate on analyzing the highest diffraction peak shift at $\sim 21.47^\circ$, which is assigned as (110) facet of CsPbBr_3 . From 0 to 50 gas injection cycles, the redshift of diffraction peak at 22.43° indicating the full substitution of Br^- with Cl^- . Figure 1f shows the steady-state photoluminescence (PL) spectra of $\text{CsPbCl}_x\text{Br}_{3-x}$ thin films under 365 nm excitation. Inset displays typical photographs of $\text{CsPbCl}_x\text{Br}_{3-x}$ thin films when 365 nm UV-LED beams illuminate the samples. The emission peak continuously blue shifts to shorter wavelength with the increasing of gas injection cycle, confirming the controllable anion-exchange reaction and band gap change. Significantly, when gas injection cycle increases to 50, the emission peak of perovskite films shifts from 525 nm to 412 nm, and the latter peak is corresponding to the excitonic signature of intrinsic CsPbCl_3 perovskites^{[[23]]}. Since Cl ion has smaller atomic radius, the Br ion in halide perovskites would be easily replaced via chemical

vapor anion-exchange reaction. The gradual substitution of Br⁻ with Cl⁻ in perovskites lattice is accounting for the shifts of diffraction peaks and PL peaks.

Next, to identify the chemical composition of anion-exchanged halide perovskites, high-resolution X-ray photoelectronic spectroscopy (XPS) spectra are measured. Figure 2(a-b) shows the high-resolution Br 3d and Cl 2p core level XPS spectra, respectively. After careful de-convolution, the Br 3d and Cl 2p core level XPS peak can be fitted into two peaks at 68.38/69.38 eV and 197.98/199.58 eV, respectively. It is interesting to note that, the doublet intensity of Br 3d XPS peak decreases with the increase of gas injection cycle. On the contrary, the converse trend is found for doublet Cl 2p core level XPS peak. In the meantime, the Cs 3d and Pb 4f XPS spectra keep unchanged (Figure S3a,b). More specifically, by quantifying the intensity of the Br 3d and Cl 2p XPS peaks, their contents varied with the gas injection cycle are extracted. With the increase of gas injection cycle, the ratio of Br/Cl for 10 cycles, 20 cycles, 50 cycles, 100 cycles are determined to be 1:0.83, 1:1.5, 1:9, 1:61, respectively. This comparison strongly supports that Br can be continuously exchanged by Cl during the gas injection cycling process. It's worth noting that the original CsPbBr₃ can in situ transforms into CsPbCl₃ after 50 gas injection cycle of anion exchange. Figure 2c shows the tendency of Br/Cl atom ratio in the mixed CsPbCl_xBr_{3-x} films, which clearly confirms the substitution can be precisely tuned by gas injection cycle. The whole anion-exchange evolution can be explained by the process of Cl⁻ replacing Br⁻ under low temperature. To figure out the element distribution in anion-exchanged perovskites, XPS depth profiling was used to analyze the chemical composition changes as a function of depth (50 cycles sample). As shown in Figure S3c, besides the presence of Cs, Pb, Cl and Br content, there also exists Ti, O, C, Sn element (Sn and O are from the FTO substrate). It indicates that the content of Ti increases with the increase of gas injection cycle (Figure S3d). To determine whether the Ti content would contribute to the anion-exchange, the Ti content as the function of etching depth was explored. Figure 3d shows the comparison of Ti_{2p} XPS spectra on the surface and

inner of sample, the largely attenuated XPS intensity in depth of 3.4 nm indicating Ti only exists on the surface of perovskites films, which in turn serves as a protection layer and contributes to the high stability of as-fabricated perovskite devices.

There is a pressing need for fabrication of uniform and high-quality bandgap tunable perovskite thin films, which is the base for high-performance thin film optoelectronic devices. The proposed vapor phase anion-exchange method can well take the above challenges for device fabrication. Figure S4 show typical SEM images of CsPbBr₃, mixed CsPbCl_xBr_{3-x} and CsPbCl₃ perovskite thin films. After 50 cycles of anion exchange, the mixed CsPbCl_xBr_{3-x} films become uniform and compact with less pinholes. However, more pinholes with smaller size would introduce after 100 gas injection cycles (Figure S4e). Based on the above structural, optical and morphology analysis, the optimal gas injection cycle for fabrication of high-quality CsPbCl₃ perovskite films is suggested to be 50. Therefore, gas injection cycle is set to be 50 for the following fabrication of UV photodetectors, which we will discuss later.

2.2 DFT Calculation and Band Structure Analysis for Anion-exchange Mechanism

To unravel the anion exchange mechanism accounting for the above structural, optical and morphology change, as well as its influence on the stability, we further used Vienna ab initio simulation package (VASP) based on density functional theory (DFT) to investigate the electronic properties systemetically.^[24] In Figure 3a, Figure 3b and Figure 3c, the projective Heyd-Scuseria-Ernzerhof (HSE03) band structures of CsPbBr₃, CsPbBr_{1.5}Cl_{1.5} and CsPbCl₃ are calculated respectively.^[25] It is obvious to see that the band gap increases from 2.28 eV to 2.79 eV when the structure changes from CsPbBr₃ to CsPbCl₃ at α -phase (Pm-3m). The total density of states (TDOS) and band gaps of CsPbBr₃, mixed CsPbCl_xBr_{3-x} and CsPbCl₃ perovskite thin films can be found in Figure 3a-c, respectively. Figure 3d shows the intriguing trend of bandgap change under different ratio of chlorine element. Herein, we applied three calculation methods for the high precision, including generalized gradient approximation

(GGA),^[26] hybrid functional Perdew-Burke-Ernzerh (PBE0)^[27] with Spin Orbital Coupling (SOC)^[28] and HSE03. Details of DOS and projective band analysis can be found in Figure S5-11. All the calculated results are in line with the experimental observations, indicating the similar trend of electronic properties. Among all the calculations, HSE03 method shows the closest bandgap values with the experimental ones, which agrees well with the above observations. Our GGA calculations is also consistent with the previously reported bandgaps of CsPbX₃ (as shown in Table S1).^[29] To better understand the electronic band structure after anion exchange, we use the schematic diagram to elucidate the bandgap increases with the bond lengths of Pb-X (inset of Figure 3d). When the Br atoms are gradually substituted by Cl atoms, the band gap of mixed halide perovskites will increase due to the longer bond length of Pb-Br (2.995 Å) than that of Pb-Cl (2.826 Å). As shown in the inset of Figure 3d, after Cl atoms substituting Br atoms, the gap value between conduction band minimum (CBM) and valence band maximum (VBM) will be enlarged, and the band gap begins to broaden. Hence, the possibility of <p|p> transition will depend on higher energy absorption due to wider band gap value in CsPbCl₃ perovskite. Additionally, to explore the stability of transformed CsPbBr₃ perovskites, the Goldschmidt tolerance factor (t) before and after Cl substitution is also calculated by the following equation^[30]: $t = (r_A + r_X) / \sqrt{2}(r_B + r_X)$, where r_A is the radius of the A cation, r_B is the radius of the B cation, and r_X is the radius of the anion. The t value gets closer to 1, the better stability of perovskites. As shown Figure 3e, the t value increases from 0.862 to 0.866, and 0.870 for CsPbBr₃, CsPbCl_{1.5}Br_{1.5} and CsPbCl₃, respectively. According to the reliable empirical index of t, the structure of transformed CsPbCl_xBr_{3-x} perovskite films is reasonable to show higher stability than that of as-grown CsPbBr₃ perovskite films. Our result is also consistent well with recent report which found chlorine mixing would enhance the stability of hybrid perovskites^[21].

2.3 Localized Anion-exchange Reaction and Confocal PL Mapping

Since the vapor-phase anion-exchange process is based on chemical diffusion, which is beneficial for large-scale transformation of perovskite thin films. The anion diffusion is chemical vapor-exposure determining step that gives rise to the gradual transformation to heterogeneous Br/Cl mixed inorganic perovskites and ultimately to CsPbCl_3 phase with wide band gap, enabling the anion-change propagation to be visualized with varied stage of gas injection cycle. Significantly, it is of great challenge to realize microscale control of the anion exchange at particular position. As a proof-of-concept study, we further employ a precision ceramic shadow mask (pore diameter $\phi=160\text{ }\mu\text{m}$) to realize microscale control of anion-exchange reaction in CsPbBr_3 perovskite films. Figure 4a shows the schematic illustration of the chemical-vapor anion-exchange process. The as-formed CsPbBr_3 perovskite films as the subjacent layer is covered by hard ceramic mask with pressure. To demonstrate the continuous stages of anion-exchange with perovskite films, we further use shadow mask by high-temperature tape on top of the ceramic mask (each piece of tape covering three columns of micropores), as shown in Figure 4b. Four different gas injection cycles (5, 15, 25, 50) are chosen, as noted I, II, III, and V, respectively. The left image shows photograph of ceramic mask, and the right image shows optical image of ceramic mask under microscopy. Figure 4c shows the fluorescence microscopy images, which can record the corresponding Cl-exchanged areas. For gas injection cycle of 5, the shadow feature of ceramic mask can be clearly identified, just like traditional lithography technology. The non-exposure area (label 1) in the center exhibits green color which is corresponding to the intrinsic color of CsPbBr_3 . As label 2 in Figure 4c, the anion-exchanged area exhibits light-blue color, indicating partial Br substitution by Cl atoms. With the increase of gas injection cycle to 15, the profile and diameter of Cl-exchanged micropores become clearer and larger, respectively. When the gas injection cycle further increase to 50, the color of anion-exchanged micropores would change to dark blue. The PL spectra also indicate the successful anion-exchange process by ALD-

chemical vapor. Figure 4d shows the diameter of micropores approximately linearly increases with the cycle number, indicating the precise control of the anion exchange process. Additionally, PL patterns of “JNU” letters illuminated by 365 nm UV LED can be clearly observed, as shown in Figure 4e. The area dark on the top is due to the tapped FTO substrate. In order to realize continuous PL images in one sample, perovskite stripes with varied gas injection cycles have been demonstrated by using high-temperature tape mask (stripe width ~1 mm). As shown in Figure 4f, it can be seen that the strip color can be continuously tuned from green to light green, dark green, then to dark blue, purple, corresponding to 0, 5, 10, 20, 30 gas injection cycles, respectively.

2.4 Wide-range and Fine-tuning Optical Absorption and General Strategy for Other Inorganic Pervoskites

Figure 5a shows the optical absorption spectra of mixed-halide perovskite films varied with gas injection cycle. The intrinsic absorption peaks show narrow and pronounced excitonic band feature, and the absorption edges blue shift from 532 nm to 416 nm with the increasing of gas injection cycle from 0 to 50 cycles. The band gaps of $\text{CsPbCl}_x\text{Br}_{3-x}$ films are calculated to be 2.33, 2.51, 2.55, 2.71, 2.82 eV and 2.98 eV, respectively (Figure S12). Benefitting from the flexibilities in controlling of experiment parameters, such as reaction temperature, gas flow rate and gas injection cycle number, the absorption peak of photoresponse layer ($\text{CsPbCl}_x\text{Br}_{3-x}$) can be precisely controlled. In order to determine the spectral resolution limit, we slow down the reaction speed by lowering the reaction temperature to room temperature. As shown in Figure 5b, the peak locates at 516.8 nm corresponding to the intrinsic absorption band of CsPbBr_3 . Under given pulse time (8 ms), the absorption peak of $\text{CsPbCl}_x\text{Br}_{3-x}$ pervoskite shifts from 515.2 nm to 513.2 nm by utilizing different gas injection cycle (2~30 cycles). The corresponding offsets are 1.6 nm, 1.2 nm and 0.8 nm, respectively. Increasing the gas injection cycle further, the absorption peak become

relative stable with minor change for the low reaction temperature. After raising the reaction temperature to 60 °C, the adsorption peak further blue shifts to 512.2 nm. Considering the wavelength accuracy (± 0.3 nm) of spectrometer, the spectral resolution limit by vapor strategy can be reasonably controlled below 1 nm. To verify the effectiveness of chemical-vapor anion-exchange reaction on other inorganic perovskites, typical Pb-based perovskite (CsPbIBr_2), Bi-based perovskite ($\text{Cs}_3\text{Bi}_2\text{Br}_9$), and double perovskite ($\text{Cs}_2\text{AgBiBr}_6$) were chosen. As shown in Figure S13(a-c), the absorption spectra of three perovskite thin films after anion exchange are compared. All the absorption edges clearly blueshift to shorter wavelength after certain ALD-assisted conversion. It can be seen that CsPbIBr_2 perovskite shows the largest shift (~ 18 nm) among them, while the $\text{Cs}_2\text{AgBiBr}_6$ exhibits the smallest shift (< 3 nm), even after 50 gas injection cycles. The offset $\Delta\lambda$ also indicates the stability of inorganic perovskites, which can experience anti-anion exchange reaction during the chemical process. Based on the above analysis, our anion-exchange method is still a general strategy for effective, precise control of the anion exchange in inorganic perovskites. The incorporation of Cl into bulk lattice would reduce the defect density, increase carrier mobility, as well as increase the stability [19, 21].

2.5 Near Ultraviolet Photodetection and Tunable Photoresponse

We have proved the high-effectivity of vapor phase for bandgap engineering of inorganic perovskites. By assistance of deposition technique, ultrathin Al_2O_3 and TiO_2 modification layers are incorporated into the interfaces between FTO and perovskites to fabricate better-performance photodetectors. Figure 6a shows typical photoresponse curves of CsPbCl_3 photodetectors measured under 405 nm laser illuminations with different power density. The heterojunction photodetectors exhibit remarkable switching characteristic between high and low conduction mode under modulated light (405 nm, 0.25 Hz). As show in Figure 6b, the photocurrent shows almost linear dependence on the light intensity in the range from 2.57

nWcm^{-2} to 5 mWcm^{-2} . The power law $I \propto P^\alpha$ was used to fit the I-P curve, and the ideal index can be calculated to be 0.89. The fitting factor is close to the ideal value of 1, implying the high-quality CsPbCl_3 thin films have low trap states. The linear dynamic range (LDR) can be determined to be 125 dB by the equation: $\text{LDR} = 20 \log(P_{\max}/P_{\min})$, where P_{\max} and P_{\min} are the maximum and minimum optical power levels measured by the PD. Benefiting from the double-side modification layers, the dark current of $\text{FTO}/\text{Al}_2\text{O}_3/\text{CsPbCl}_3/\text{TiO}_2$ (ACT) PDs can be suppressed to the lowest level of 10^{-11} A , along with the detectable limit of 2.57 nWcm^{-2} , as shown in Figure S14a. Besides, the UV photodetectors also exhibit fast response speed, with rise time and decay time of 7 ms and 165 ms, respectively (Figure S14b). The specific detectivity is an important parameters for evaluating the weak light detecting capability of ACT PDs, which can be calculated by $D^* = R/(2qJ_d)^{1/2}$, where R is responsivity, and J_d is dark current density. As plotted in Figure 6c, R and D^* decrease almost linearly with the increase of light intensity in the range from 2.57 nWcm^{-2} to 5 mWcm^{-2} . The highest R of 0.1 AW^{-1} can be obtained. The specific detectivity D^* is determined to be as high as $3.28 \times 10^{12} \text{ Jones}$ (@405 nm). Furthermore, the spectral response curves of perovskite PDs with different gas injection cycles were also measured. As shown in Figure 6d, the CsPbBr_3 PDs show a broader response range with high sensitivity located at 520 nm, which corresponding to the adsorption edge of CsPbBr_3 (Figure 5a). After 10 cycles of ALD-assisted anion exchange, partial Br atoms would be replaced by Cl atoms and forming mixed perovskites, the photoresponse edge would blueshift to 490 nm for the broadening band gap. When the gas injection cycle increases to 20 and 50, the photoresponse edge would further blueshifts to 460 and 429 nm, respectively. Based on aforementioned adsorption measurement, the mixed pervoskites would fully converse to CsPbCl_3 after 50 gas injection cycles. Therefore, the response spectrum range corresponds to the absorption band gap of CsPbCl_3 . It's worth mentioning that, the photoresponse range can be easily tuned from visible to ultraviolet by precise control of the gas injection cycle. The interval of the cutoff response edge is around 30 nm which is

associated with above adsorption spectra, revealing a high spectra resolution of ~30 nm can be achieved using the devices. The wafer area could be easily scaled up by the anion-exchange method, together with interfacial engineering, strengthen the competitiveness of all inorganic perovskite-based UV optoelectronic applications.

3. Conclusion

In this work, through novel in situ conversion method, we have successfully established a universal low-temperature chemical-vapor anion-exchange strategy for exchange halogen anions in inorganic perovskites. During the vapor-phase reaction process, Br atoms can be gradually substituted by Cl atoms, which have been confirmed by optical absorption, XRD and XPS characterization. DFT calculations is employed to unveil the experimental results and show the consistent trends on tuning the optoelectronic properties by changing the halide anions. Significantly, high-quality and large-scale uniform CsPbCl₃ perovskite thin films are obtained for the first time. Tunable photoresponse from green to near ultraviolet light ($\Delta\lambda \sim 100$ nm) can be realized by our strategy, along with a remarkable spectral resolution of ~1 nm. Our general method can be extended to other inorganic perovskites including Pb-based perovskite (CsPbIBr₂), Bi-based perovskite (Cs₃Bi₂Br₉), and double perovskite (Cs₂AgBiBr₆). The wafer-area anion-exchange method, together with interfacial engineering, would strengthen the competitiveness of perovskite photodetectors with tunable response range, which has great potential application in the fields of machine vision and artificial vision.

4. Methods

Materials synthesis: The FTO glass substrates were sequentially washed with isopropanol, acetone, ionized water and isopropanol for 15 min, respectively. The sheet resistance of FTO is 15 $\Omega \square^{-1}$. After that, the cleaned substrates were dried by nitrogen flow, and following was treated by UV-ozone cleaner for 30 min. Then, the as-prepared substrates were put into atomic layer deposition system (ALD, Beneq TFS200) for following ALD-

modification layer deposition. Aluminium trimethide (TMA) and H₂O were precursors, and high purity nitrogen was used as the carrier gas. The thickness of ALD-layer can be precisely controlled by adjusting the cycling number (growth rate=0.09 nm/cycle). For the growth of ALD-Al₂O₃ layer, the cycling number is set to be 16 under 85 °C for 5 min, corresponding to an optimal thickness of 1.5 nm ^{[[22]]}. After that, the CsPbBr₃ thin films were spin-coated on the ALD-Al₂O₃ modified FTO substrate at room temperature. First, 0.4 mol CsBr and 0.4 mol PbBr₂ were mixed and dissolved in 1 mL of dimethyl sulfoxide (DMSO) solution, which was stirred on a hot plate (70 °C).

Vapor-phase halogen exchange: Afterward, the precursor solution was spin coated onto the as-prepared substrates (FTO and ALD-Al₂O₃ coated FTO), the spin-coating parameters are set to be 500 rpm for 6 s and 4000 rpm for 30 s. The vapor-phase halogen reaction was performed in chamber (105 °C, 9 Pa). Titanium tetrachloride (TiCl₄) as precursors were purged on perovskites surface, and high purity nitrogen was used as carrier gas. The content of TiCl₄ gas per cycle is 200 ppm, and the N₂ purge time is 2s.

Devices fabrication: After the synthesis of CsPbBr₃ thin films, ultrathin layer of TiO₂ were further deposited on the CsPbBr₃ perovskite thin films by ALD technique. Titanium tetrachloride (TiCl₄) and H₂O were precursors, and high purity nitrogen was used as carrier gas. The growth rate was 0.06 nm per cycle at 105 °C for 17 min. Thickness of TiO₂ layers were controlled by adjusting the cycle numbers. After the deposition of dense and compacted TiO₂ layers, 100 nm Au electrode was deposited on the front of TiO₂ layer by thermal evaporation method (4×10^{-4} Pa).

Materials characterization: The structure for CsPbBr₃ perovskite thin films was characterized by X-ray diffraction (XRD) technique (Rigaku, Miniflex600). The energy band alignments are measured by ultraviolet photoelectron spectra (UPS, He I radiation, $h\nu=21.22$ eV). All the samples were biased with -5 V to obtain the low energy secondary electron (SE) cutoffs. The optical absorption spectra of CsPbBr₃ perovskite films were characterized by

UV-Vis spectrophotometer (SHIMADZU, UV-2600). Photoluminescence (PL) spectra of CsPbBr₃ perovskite thin films were obtained from photoluminescence spectroscopy (SHIMADZU, RF-5301PC). The SEM images of CsPbBr₃ perovskite film were obtained by using scanning electron microscope (SEM, ZEISS ULTRA 55). PL mapping was visualized using a Zeiss confocal fluorescence microscope (ZEISS, LSM700) and quantified with software.

DFT calculation: Density Functional Theory (DFT) Calculations. The calculation based on density functional theory (DFT) was carried out using Vienna ab initio simulation package (VASP).^[24] Herein, we used the projector augmented waves (PAW)^[31] as the pseudopotentials. The band structures and Density of States (DOS) were calculated by employing the Perdew–Burke-Ernzerh (PBE)^[26] of the generalized gradient approximation (GGA) as the exchange-correlation functional. In addition, four high-symmetric k-points: Γ (0, 0, 0), X (0, 1/2, 0), M (1/2, 1/2, 0), and R (1/2, 1/2, 1/2) were included when we calculate the band structures. We chose 6×6×6 k-point mesh for the Brillouin zone.^[32] The plane-wave cutoff energy of wave function was set as 400 eV. A 2×2×2 supercell including 40 atoms is used for the CsPbBr_{1.5}Cl_{1.5} calculations. To get the accurate bandgap, we used the Heyd-Scuseria-Ernzerhof (HSE) hybrid functional^[25] containing HSE03 and HSE06 for the further calculation. Meanwhile, we utilized the hybrid functional PBE0^[27] and found the similar band structures with overestimated values. Noticeably, all our calculations show the same trend of band gaps, especially for HSE03 method, whose theoretical band gaps are in good agreement with the experimental values.

Photoresponse measurement: To evaluate the photoresponse performance of CsPbBr₃ perovskite PDs, the I-V curves and photoresponse curves were measured by Keithley source meter (2601A). The monochrome light is 405 nm laser sources, the intensity is calibrated by a standard Si power meter (LE-LPM-HS411). The time-dependent photocurrent curves were measured under illumination of 405 nm light. The output power could be adjusted and

controlled by neutral optical attenuation plates. The transient photoresponse behavior of the PDs is measured using the photo-induced open-circuit voltage decay method under a pulsed laser (405 nm). Photoresponse speeds of the PDs were evaluated by combining a pulse laser and a digital oscilloscope (Tektronix MSO 3054, 500 MHz). The spectral response (300-1100 nm) curve of the PDs is measured using a QE-R external quantum efficiency instrument (Enlitech, Si detector S10-14010), and the photocurrent is recorded by a Keithley 2601A source meter.

Supporting Information

Supporting Information is available from the Wiley Online Library or from the author.

Acknowledgements

Guobiao Cen and Yufan Xia contributed equally to this work. This work was supported by the National Natural Science Foundation of China (Grant Nos. 61604061, 51772135, 11804117 and 11774079), the Natural Science Foundation of Guangdong Province, China (Grant Nos. 2019A1515010482, 2020A1515011377), the Fundamental Research Funds for the Central Universities (Grant No. 21618405). We also thank Prof. Dong Ma and Dr. Qikun Cheng, Gai Wang for performing the conformal PL imaging measurement at Jinan University, Dr. Huawei Song, Chunhua Su for performing the TEM measurements at Sun Yat-sen University.

Received: ((will be filled in by the editorial staff))

Revised: ((will be filled in by the editorial staff))

Published online: ((will be filled in by the editorial staff))

References

- [1] a) X. Tang, M. M. Ackerman, M. Chen, P. Guyot-Sionnest, *Nat. Photonics* **2019**, 13, 277; b) Z. Yang, T. Albrow-Owen, H. Cui, J. Alexander-Webber, F. Gu, X. Wang, T.-C. Wu, M. Zhuge, C. Williams, P. Wang, A. V. Zayats, W. Cai, L. Dai, S. Hofmann, M. Overend, L. Tong, Q. Yang, Z. Sun, T. Hasan, *Science* **2019**, 365, 1017.
- [2] C. Sun, M. T. Wade, Y. Lee, J. S. Orcutt, L. Alloatti, M. S. Georgas, A. S. Waterman, J. M. Shainline, R. R. Avizienis, S. Lin, B. R. Moss, R. Kumar, F. Pavanello, A. H. Atabaki, H. M. Cook, A. J. Ou, J. C. Leu, Y.-H. Chen, K. Asanović, R. J. Ram, M. A. Popović, V. M. Stojanović, *Nature* **2015**, 528, 534.
- [3] R. D. Jansen-van Vuuren, A. Armin, A. K. Pandey, P. L. Burn, P. Meredith, *Adv. Mater.* **2016**, 28, 4766.
- [4] J. Xue, Z. Zhu, X. Xu, Y. Gu, S. Wang, L. Xu, Y. Zou, J. Song, H. Zeng, Q. Chen, *Nano Lett.* **2018**, 18, 7628.
- [5] F. Yesilkoy, E. R. Arvelo, Y. Jahani, M. Liu, A. Tittl, V. Cevher, Y. Kivshar, H. Altug,

- Nat. Photonics* **2019**, 13, 390.
- [6] F. P. García de Arquer, A. Armin, P. Meredith, E. H. Sargent, *Nat. Rev. Mater.* **2017**, 2.
 - [7] L. Dou, M. Lai, C. S. Kley, Y. Yang, C. G. Bischak, D. Zhang, S. W. Eaton, N. S. Ginsberg, P. Yang, *Proc. Natl. Acad. Sci. U. S. A.* **2017**, 114, 7216.
 - [8] a) Y. Fang, Q. Dong, Y. Shao, Y. Yuan, J. Huang, *Nature Photonics* **2015**, 9, 679; b) J. B. Rivest, P. K. Jain, *Chem. Soc. Rev.* **2013**, 42, 89.
 - [9] T. Leijtens, K. A. Bush, R. Prasanna, M. D. McGehee, *Nat. Energy* **2018**, 3, 828.
 - [10] D. Zhang, Y. Yang, Y. Bekenstein, Y. Yu, N. A. Gibson, A. B. Wong, S. W. Eaton, N. Kornienko, Q. Kong, M. Lai, A. P. Alivisatos, S. R. Leone, P. Yang, *J. Am. Chem. Soc.* **2016**, 138, 7236.
 - [11] a) G. Nedelcu, L. Protesescu, S. Yakunin, M. I. Bodnarchuk, M. J. Grotevent, M. V. Kovalenko, *Nano Lett.* **2015**, 15, 5635; b) S. Dastidar, D. A. Egger, L. Z. Tan, S. B. Cromer, A. D. Dillon, S. Liu, L. Kronik, A. M. Rappe, A. T. Fafarman, *Nano Lett.* **2016**, 16, 3563.
 - [12] S. E. Creutz, H. Liu, M. E. Kaiser, X. Li, D. R. Gamelin, *Chem. Mater.* **2019**, 31, 4685.
 - [13] D. Parobek, Y. Dong, T. Qiao, D. Rossi, D. H. Son, *J. Am. Chem. Soc.* **2017**, 139, 4358.
 - [14] a) Y.-C. Chen, H.-L. Chou, J.-C. Lin, Y.-C. Lee, C.-W. Pao, J.-L. Chen, C.-C. Chang, R.-Y. Chi, T.-R. Kuo, C.-W. Lu, D.-Y. Wang, *J. Phys. Chem. C* **2019**, 123, 2353; b) K. Abdel-Latif, R. W. Epps, C. B. Kerr, C. M. Papa, F. N. Castellano, M. Abolhasani, *Adv. Funct. Mater.* **2019**, 29, 1900712.
 - [15] a) G. H. Ahmed, J. Yin, R. Bose, L. Sinatra, E. Alarousu, E. Yengel, N. M. AlYami, M. I. Saidaminov, Y. Zhang, M. N. Hedhili, O. M. Bakr, J.-L. Brédas, O. F. Mohammed, *Chem. Mater.* **2017**, 29, 4393; b) J. De Roo, M. Ibáñez, P. Geiregat, G. Nedelcu, W. Walravens, J. Maes, J. C. Martins, I. Van Driessche, M. V. Kovalenko, Z. Hens, *ACS Nano* **2016**, 10, 2071; c) A. Pan, B. He, X. Fan, Z. Liu, J. J. Urban, A. P. Alivisatos, L. He, Y. Liu, *ACS Nano* **2016**, 10, 7943.
 - [16] L. Protesescu, S. Yakunin, M. I. Bodnarchuk, F. Krieg, R. Caputo, C. H. Hendon, R. X. Yang, A. Walsh, M. V. Kovalenko, *Nano Lett.* **2015**, 15, 3692.
 - [17] W. Zheng, P. Huang, Z. Gong, D. Tu, J. Xu, Q. Zou, R. Li, W. You, J.-C. G. Bünzli, X. Chen, *Nat. Commun.* **2018**, 9, 3462.
 - [18] H. Tan, A. Jain, O. Voznyy, X. Lan, F. P. García de Arquer, J. Z. Fan, R. Quintero-Bermudez, M. Yuan, B. Zhang, Y. Zhao, F. Fan, P. Li, L. N. Quan, Y. Zhao, Z.-H. Lu, Z. Yang, S. Hoogland, E. H. Sargent, *Science* **2017**, 355, 722.
 - [19] J. Xu, C. C. Boyd, J. Y. Zhengshan, A. F. Palmstrom, D. J. Witter, B. W. Larson, R. M. France, J. Werner, S. P. Harvey, E. J. Wolf, *Science* **2020**, 367, 1097.
 - [20] a) D. Parobek, Y. Dong, T. Qiao, D. Rossi, D. H. Son, *J. Am. Chem. Soc.* **2017**, 139, 4358; b) Z.-J. Li, E. Hofman, A. H. Davis, M. M. Maye, W. Zheng, *Chem. Mater.* **2018**, 30, 3854.
 - [21] N. Rybin, D. Ghosh, J. Tisdale, S. Shrestha, M. Yoho, D. Vo, J. Even, C. Katan, W. Nie, A. J. Neukirch, S. Tretiak, *Chem. Mater.* **2020**, 32, 1854.
 - [22] G. Cen, Y. Liu, C. Zhao, G. Wang, Y. Fu, G. Yan, Y. Yuan, C. Su, Z. Zhao, W. Mai, *Small* **2019**, 15, 1902135.
 - [23] L. Protesescu, S. Yakunin, M. I. Bodnarchuk, F. Krieg, R. Caputo, C. H. Hendon, R. X. Yang, A. Walsh, M. V. Kovalenko, *Nano Lett.* **2015**, 15, 3692.
 - [24] G. Kresse, J. Furthmüller, *Phys. Rev. B* **1996**, 54, 11169.
 - [25] J. Heyd, G. E. Scuseria, M. Ernzerhof, *J. Chem. Phys.* **2003**, 118, 8207.
 - [26] J. P. Perdew, K. Burke, M. Ernzerhof, *Phys. Rev. Lett.* **1996**, 77, 3865.
 - [27] C. Adamo, V. Barone, *J. Chem. Phys.* **1999**, 110, 6158.
 - [28] a) J. Even, L. Pedesseau, J.-M. Jancu, C. Katan, *J. Phys. Chem. Lett.* **2013**, 4, 2999; b)

- E. Narsimha Rao, G. Vaitheeswaran, A. H. Reshak, S. Auluck, *Phys. Chem. Chem. Phys.* **2017**, 19, 31255.
- [29] M. Ahmad, G. Rehman, L. Ali, M. Shafiq, R. Iqbal, R. Ahmad, T. Khan, S. Jalali-Asadabadi, M. Maqbool, I. Ahmad, *J. Alloys Compd.* **2017**, 705, 828.
- [30] Z. Li, M. Yang, J.-S. Park, S.-H. Wei, J. J. Berry, K. Zhu, *Chem. Mater.* **2016**, 28, 284.
- [31] G. Kresse, D. Joubert, *Phys. Rev. B* **1999**, 59, 1758.
- [32] J. D. Pack, H. J. Monkhorst, *Phys. Rev. B* **1977**, 16, 1748.

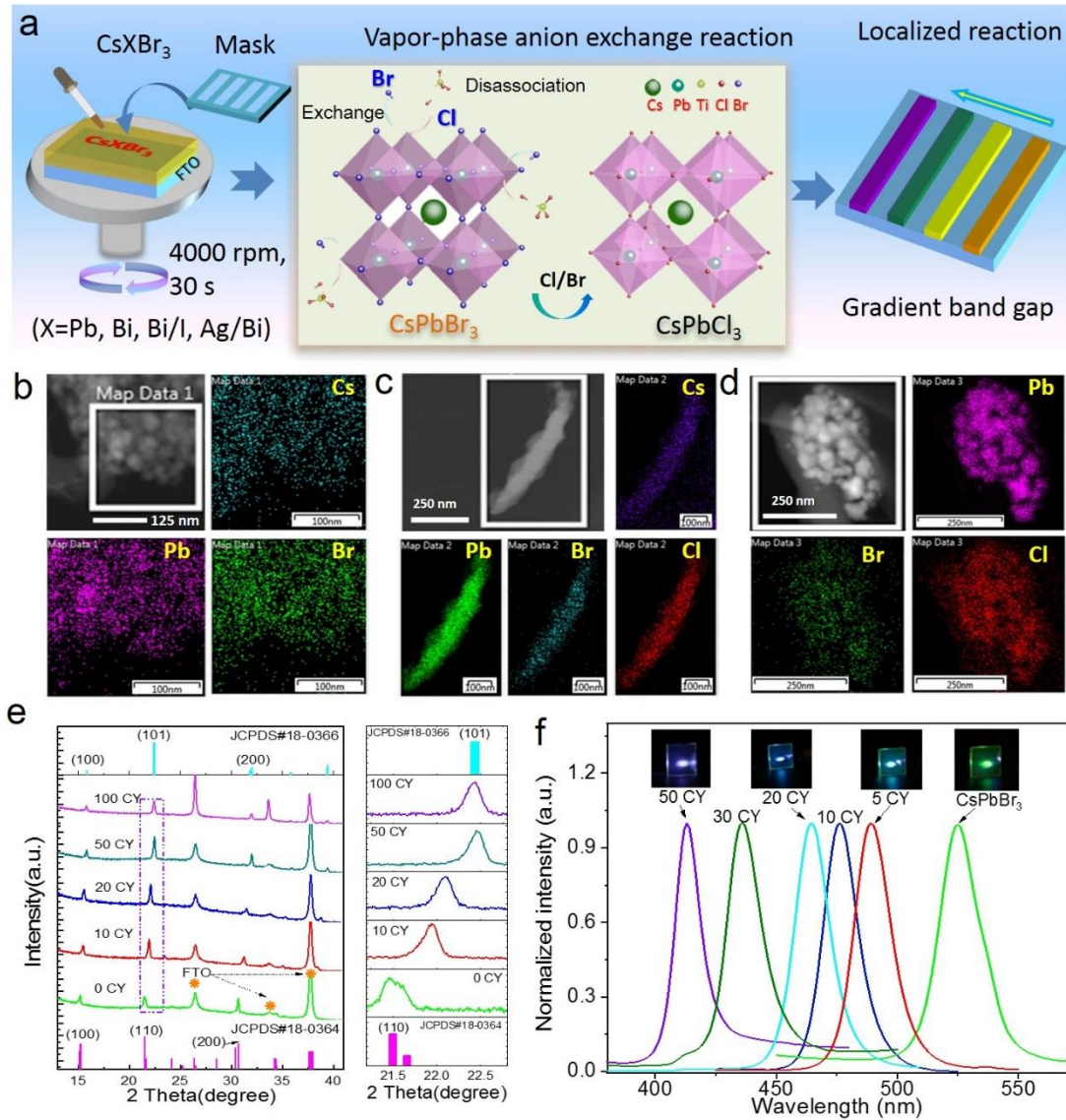


Figure 1. Characterizations of chemical-vapor anion-exchange samples. (a) Schematic of vapor-phase anion-exchange reaction, (b-d) TEM-EDS mapping of Cs, Pb, Br, Cl components of cesium lead halide perovskites with varied gas injection cycling number of 0, 20, and 50, respectively, (e) Comparison of XRD patterns of original CsPbBr₃ films and anion-exchanged CsPbCl_xBr_{3-x} films, (f) Corresponding photoluminescence spectra. Insets of Figure 1g show the photos of the perovskite films under UV irradiation (λ=365 nm).

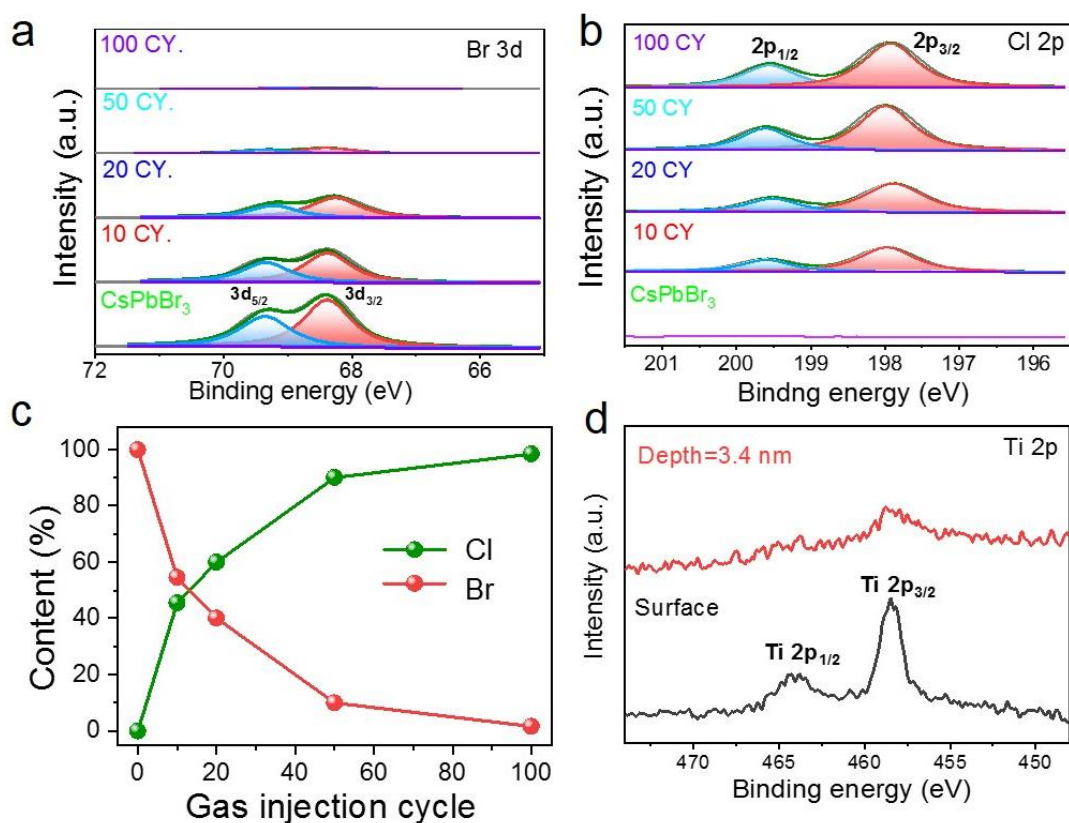


Figure 2. XPS characterization of cesium lead halide perovskites with varied gas injection cycle. (a) Br 3d core level XPS spectra, (b) Cl 2p core level XPS spectra, (c) Cl/Br content varied with the gas injection cycle, (d) XPS depth profiling of Ti 2p content on the surface and 3.4 nm below surface.

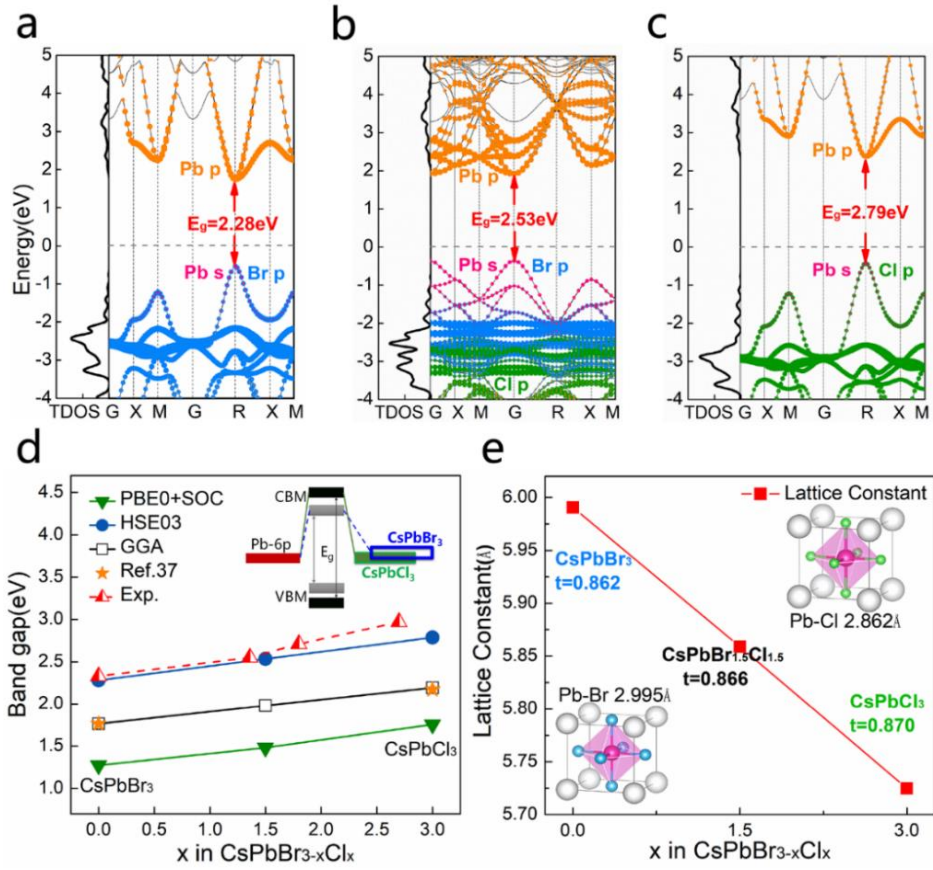


Figure 3. DFT Calculation of Electronic Properties and Band-Trend Analysis. DOS and projective band structure based on HSE03 method of (a) CsPbBr₃ perovskite, (b) CsPbCl_{1.5}Br_{1.5} perovskite, (c) CsPbCl₃ perovskite, (d) Trend of calculated band gaps of CsPbCl_xBr_{3-x} as a function of composition x of halide anions, inset gives the schematic diagram of band change due to anion exchange. (e) The calculated tolerance factor and lattice constant before and after Cl substitution.

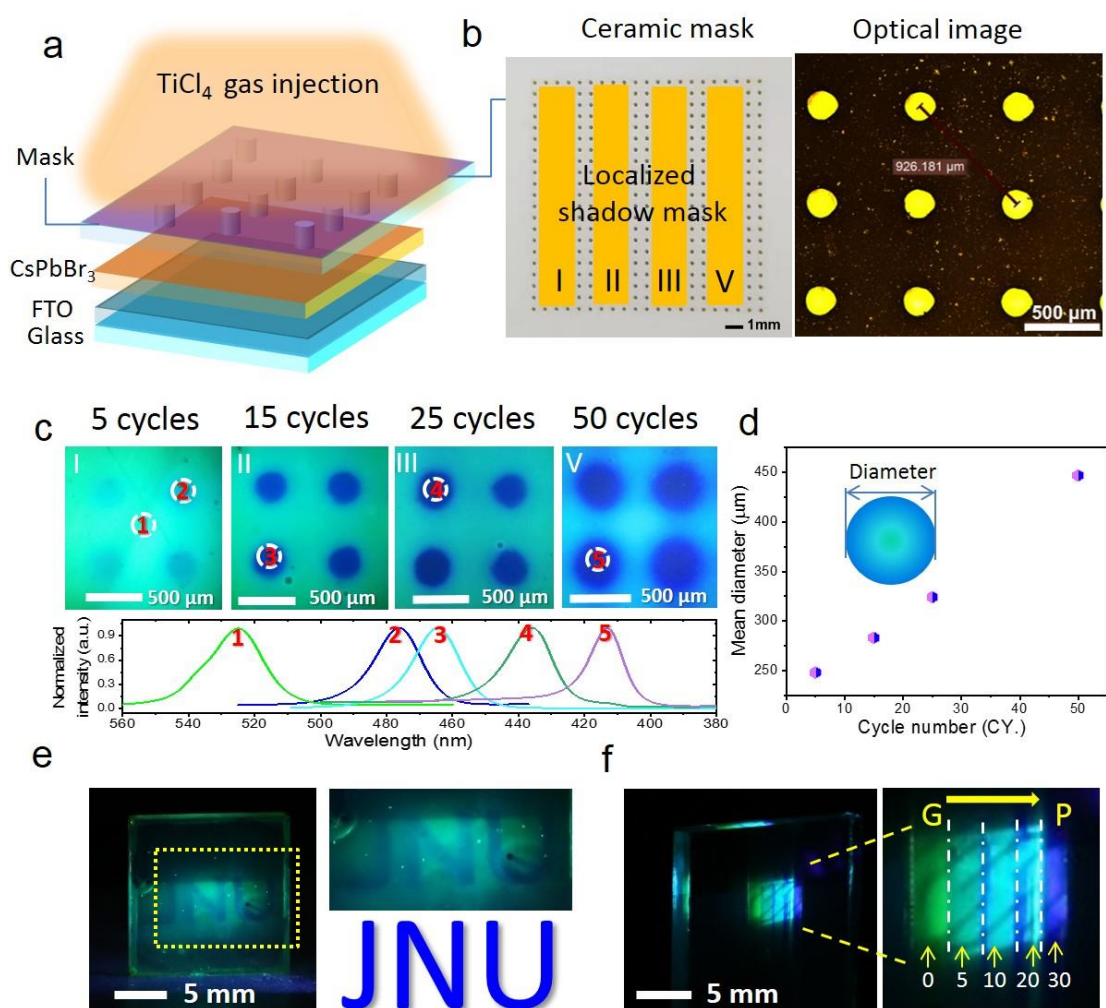


Figure 4. Localized Anion-exchange Reaction and Confocal PL Mapping. (a) A schematic illustration of the anion-exchange process. (b) ceramic mask and its optical image. (c) PL mapping of localized anion-exchanged areas with varied cycles. (d) Diameter of micropore varied with cycle number. (e) PL images of letters "JNU" and (f) strips under 365 nm excitation.

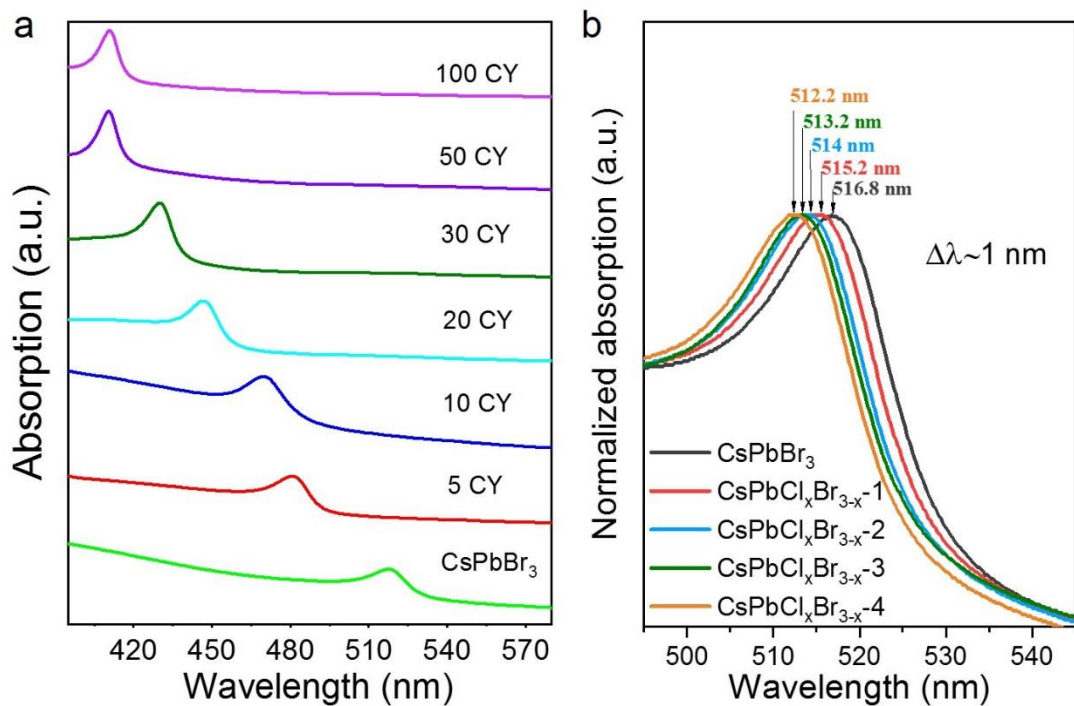


Figure 5. Wide-range and Fine-tuning Optical Absorption of CsPbCl_xBr_{3-x} perovskites. (a) Typical optical adsorption spectra by utilizing different cycles, (b) Fine-tuning adsorption spectra of CsPbCl_xBr_{3-x} films under different cycles.

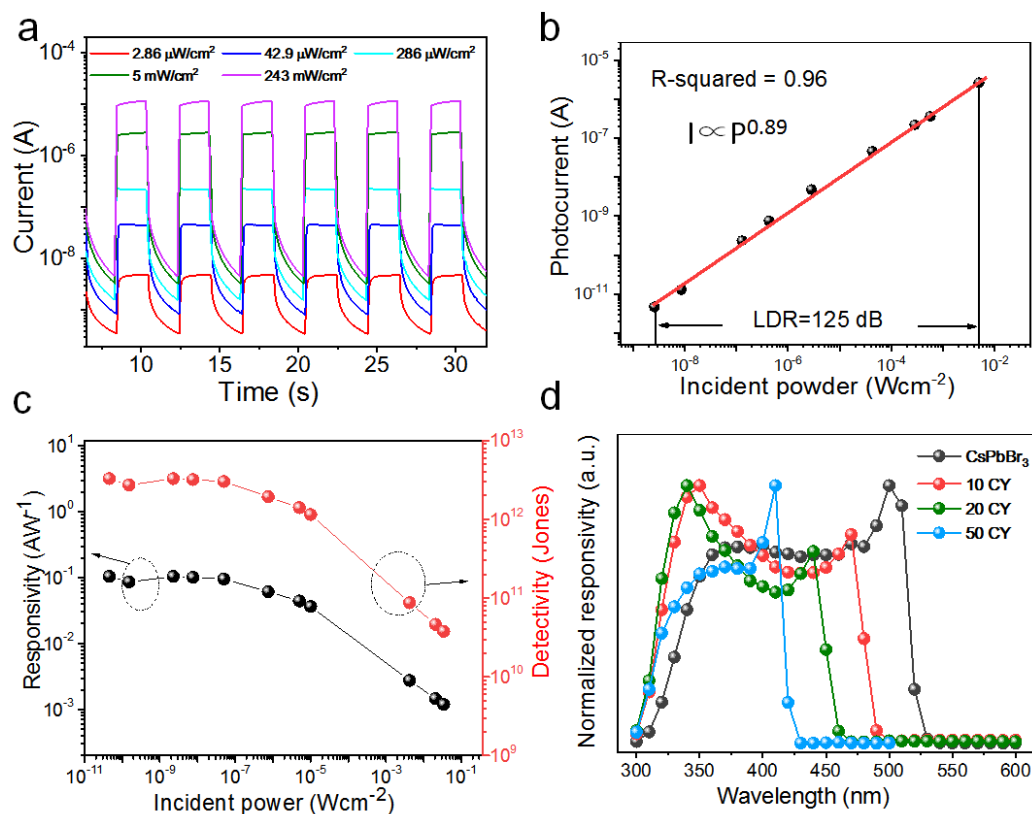
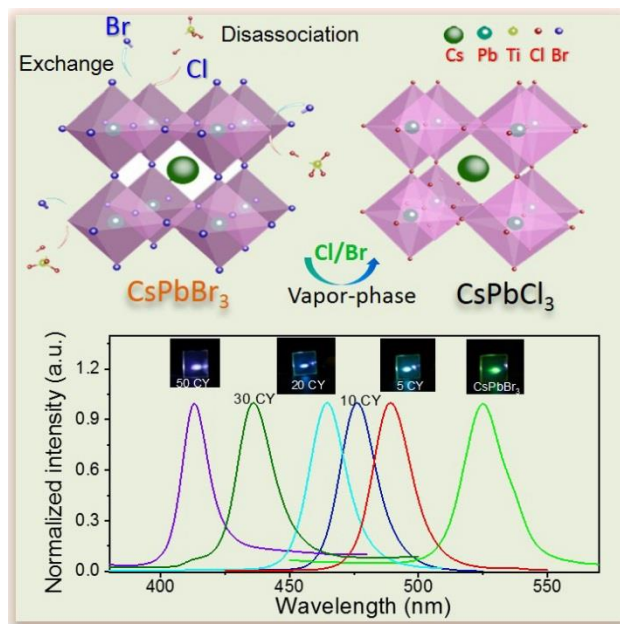


Figure 6. UV detection performance of CsPbCl₃ PDs. (a) Typical photoresponse curves under 405 nm illumination with different power density. (b) Corresponding linear dynamic range. (c) Power-dependent responsivity and specific detectivity curve, (d) photoresponse spectra by different anion-exchange process.

Precise phase control of large-scale inorganic perovskites via vapor-phase anion-exchange strategy

ToC figure ((Please choose one size: 55 mm broad \times 50 mm high **or** 110 mm broad \times 20 mm high. Please do not use any other dimensions))



Supporting Information

Precise phase control of large-scale inorganic perovskites via vapor-phase anion-exchange strategy

Guobiao Cen^{#1}, Yufan Xia^{#1}, Chuanxi Zhao^{1*}, Yong Fu¹, Yipeng An², Ye Yuan¹, Tingting Shi^{1*}, Wenjie Mai^{1*}

¹Siyuan Laboratory, Guangdong Provincial Engineering Technology Research Center of Vacuum Coating Technologies and New Energy Materials, Department of Physics, Jinan University, Guangzhou, Guangdong 510632, People's Republic of China.

²School of Physics & International United Henan Key Laboratory of Boron Chemistry and Advanced Energy Materials, Henan Normal University, Xinxiang, Henan 453007, China.

Contents

Figure S1. Solubility of perovskites precursor.

Figure S2. EDS characterization.

Figure S3. XPS spectra of Cs3d, Pb2f and Ti2p and XPS depth profile

Figure S4. SEM images of perovskites with different ALD cycles

Figure S5. The density of states (DOS) from (a) CsPbBr₃, (b) CsPbBr_{1.5}Cl_{1.5} and (c)CsPbCl₃.

Figure S6. HSE03 projective band of (a) CsPbBr₃:Pb and (b) CsPbBr₃:Br.

Figure S7. HSE03 projective band of (a) CsPbBr_{1.5}Cl_{1.5}:Pb, (b) CsPbBr_{1.5}Cl_{1.5}:Br and (c) CsPbBr_{1.5}Cl_{1.5}:Cl.

Figure S8. HSE03 projective band of (a) CsPbCl₃:Pb and (b)CsPbCl₃:Cl.

Figure S9. GGA projective band of (a) CsPbBr₃:Pb and (b)CsPbBr₃:Br.

Figure S10. GGA projective band of (a) CsPbBr_{1.5}Cl_{1.5}:Pb, (b) CsPbBr_{1.5}Cl_{1.5}:Br and (c) CsPbBr_{1.5}Cl_{1.5}:Cl.

Figure S11. GGA projective band of (a) CsPbCl₃:Pb and (b) CsPbCl₃:Cl.

Figure S12. Absorption spectra of perovskites

Figure S13. General strategy for other inorganic perovskites thin films.

Figure S14. The detection limit and photoresponse speed of CsPbCl₃ UV PDs.

Table S1. Comparison of the calculated and reported bandgaps of CsPbX₃

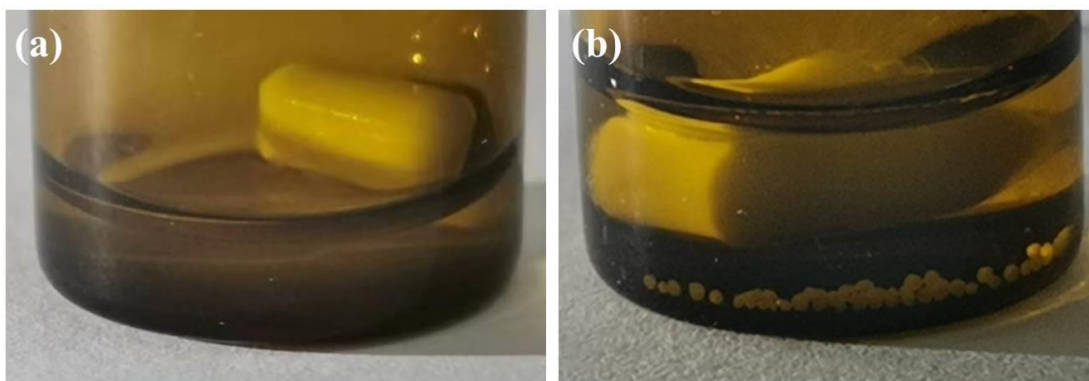


Figure S1. Solubility of perovskites precursors (stirred for 6 hours). (a) 0.4 M CsPbBr_3 precursor. (b) 0.1 M CsPbCl_3 precursor.

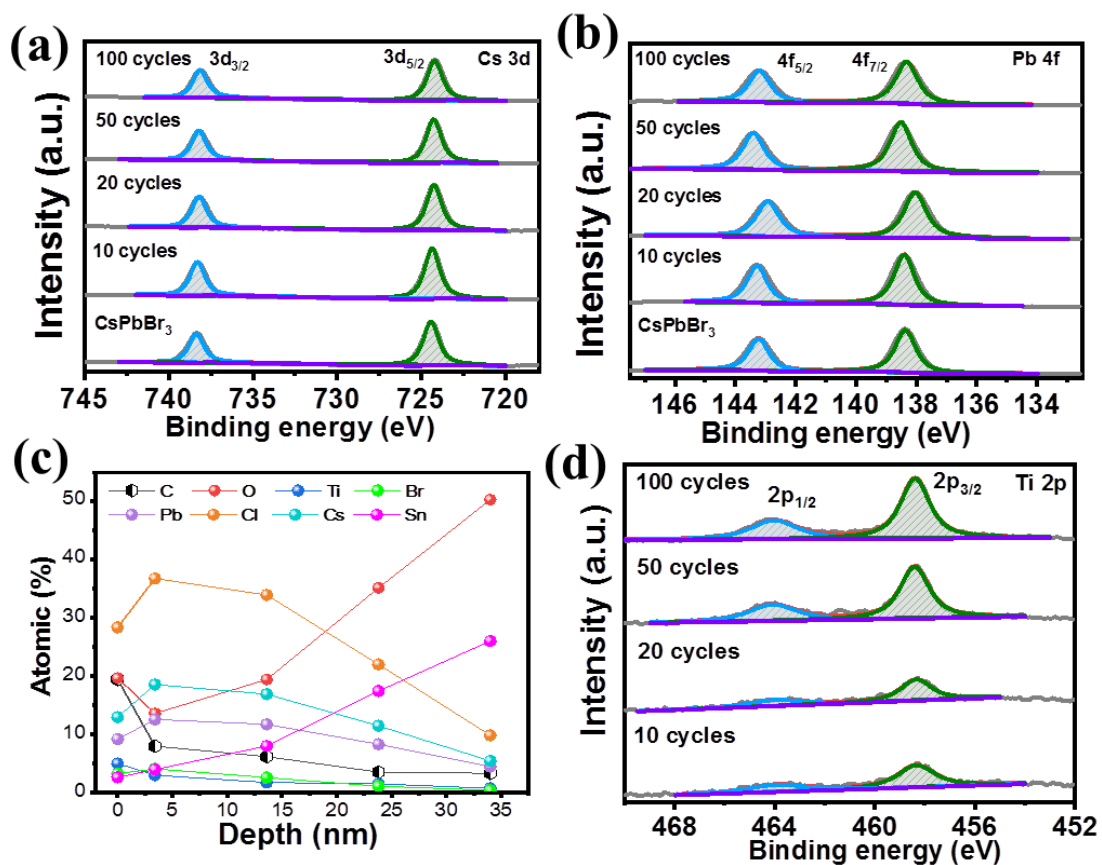


Figure S3. High resolution XPS spectra of (a) Cs 3d, (b) Pb 2f and (c) XPS depth profiles, (d) Ti 2p for perovskites under different ALD cycles.

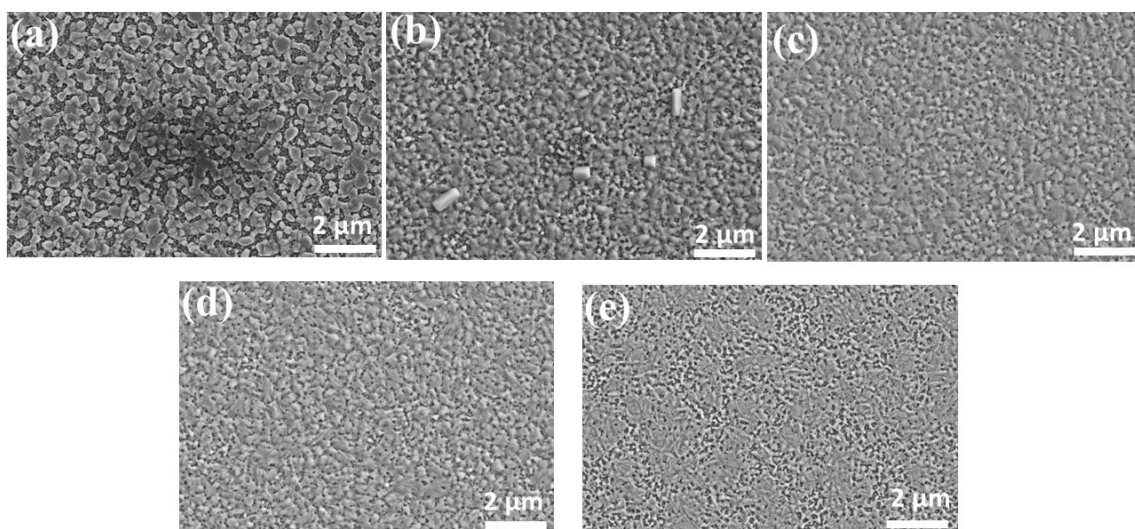


Figure S4. SEM images of perovskites under different gas injection cycle. (a) 0 cycle, (b) 10 cycles, (c) 20 cycles, (d) 50 cycles, (e) 100 cycles

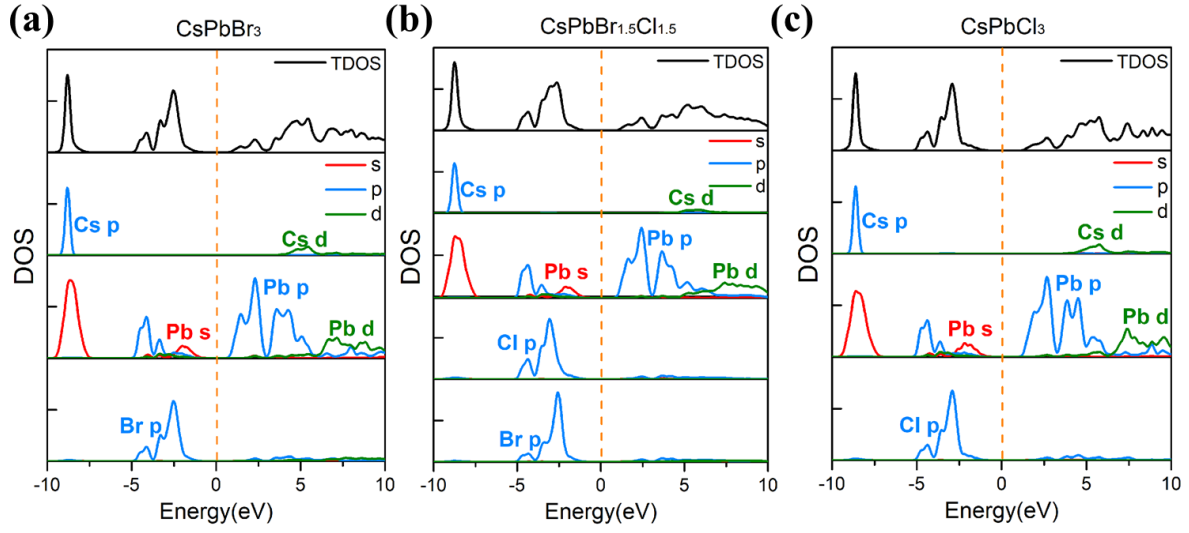


Figure S5. The density of states (DOS) from (a) CsPbBr₃, (b) CsPbBr_{1.5}Cl_{1.5} and (c) CsPbCl₃.

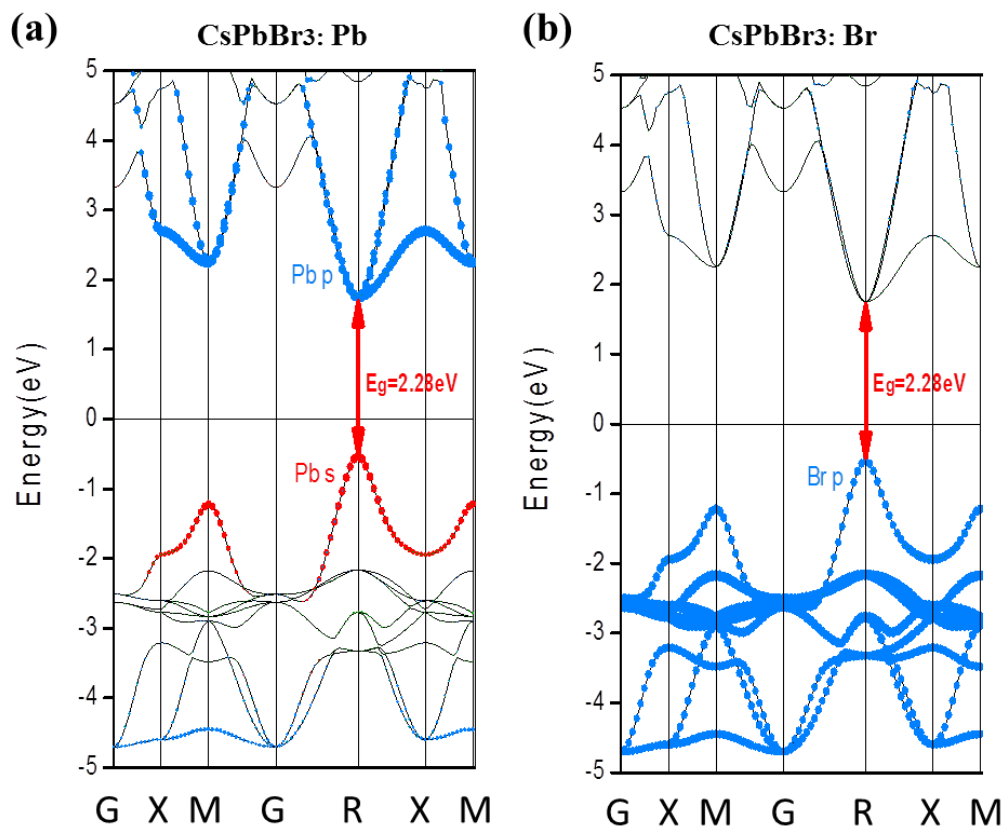


Figure S6. HSE03 projective band of (a) CsPbBr₃:Pb and (b) CsPbBr₃:Br

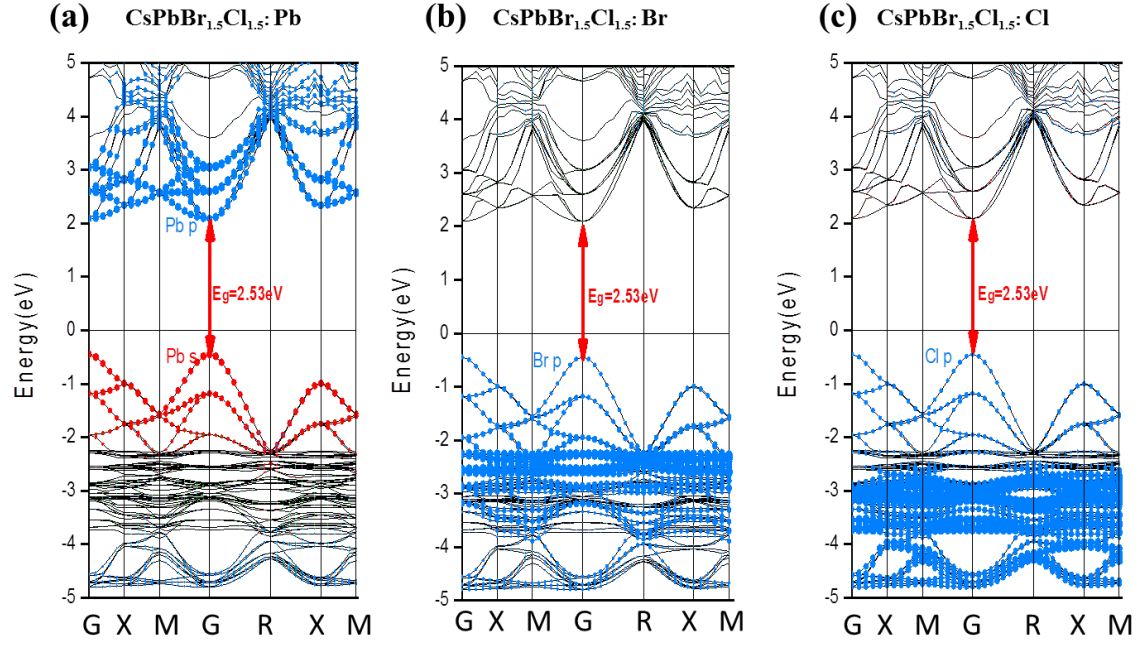


Figure S7. HSE03 projective band of (a) $\text{CsPbBr}_{1.5}\text{Cl}_{1.5}:\text{Pb}$, (b) $\text{CsPbBr}_{1.5}\text{Cl}_{1.5}:\text{Br}$ and (c) $\text{CsPbBr}_{1.5}\text{Cl}_{1.5}:\text{Cl}$.

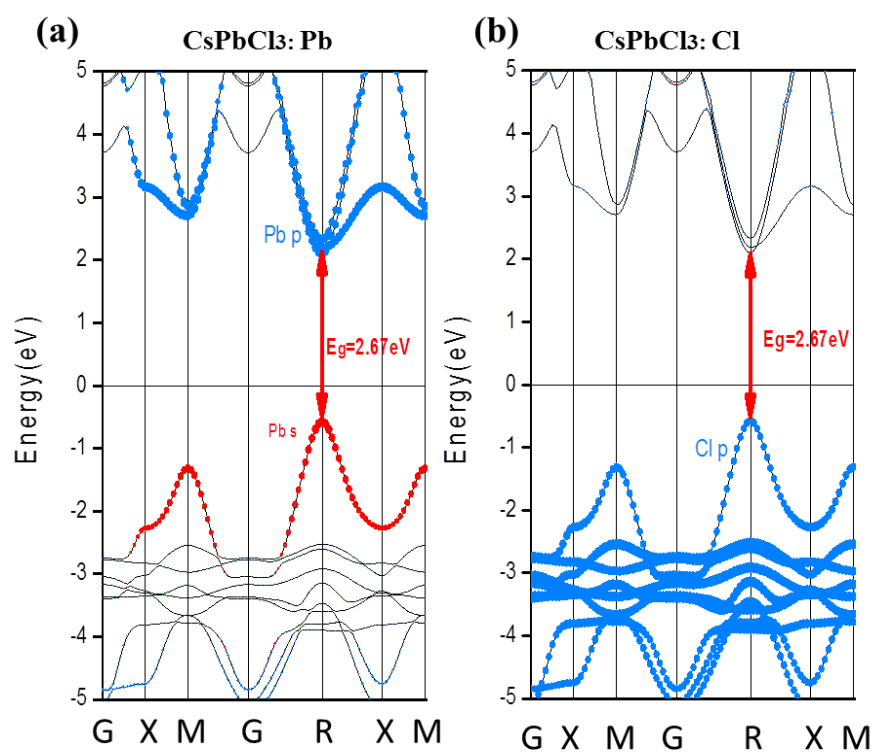


Figure S8. HSE03 projective band of (a) CsPbCl₃:Pb and (b) CsPbCl₃:Cl.

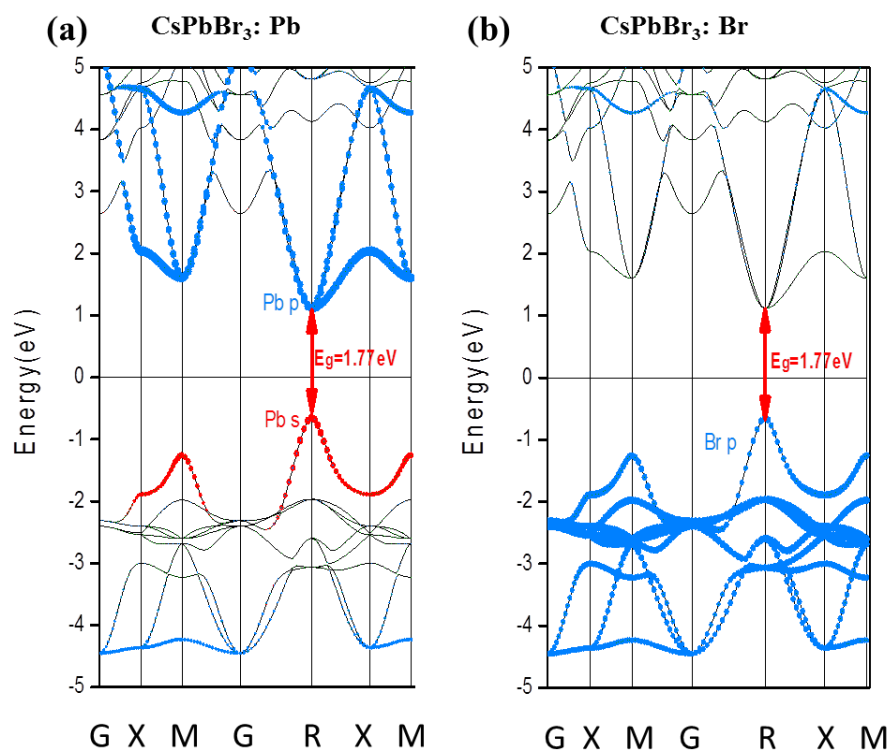


Figure S9. GGA projective band of (a) CsPbBr₃:Pb and (b) CsPbBr₃:Br.

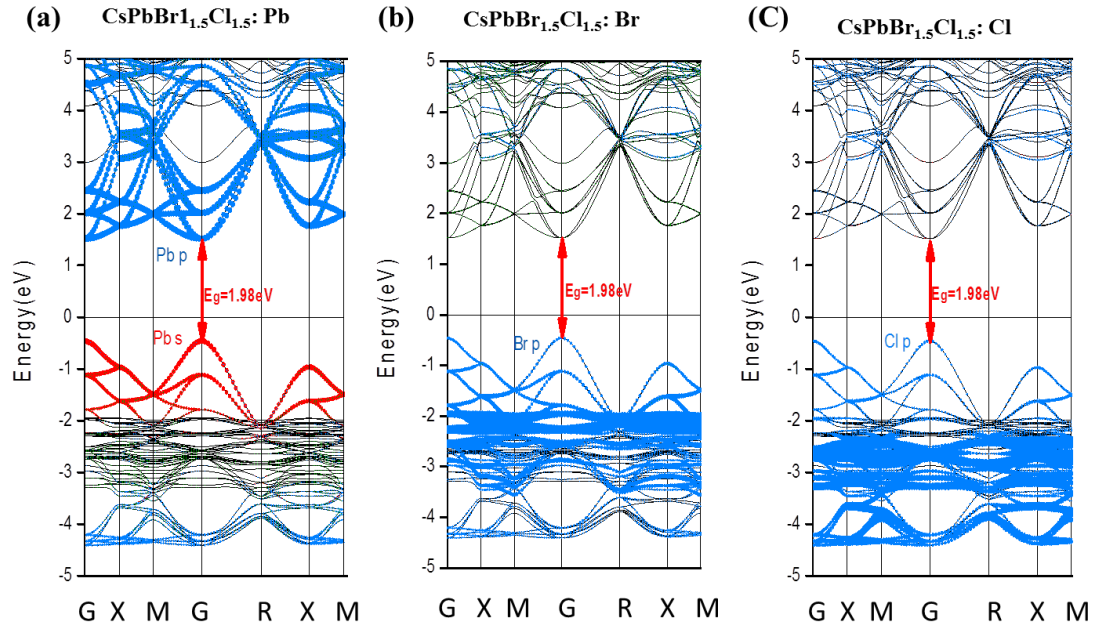


Figure S10. GGA projective band of (a) $\text{CsPbBr}_{1.5}\text{Cl}_{1.5}:\text{Pb}$, (b) $\text{CsPbBr}_{1.5}\text{Cl}_{1.5}:\text{Br}$ and (c) $\text{CsPbBr}_{1.5}\text{Cl}_{1.5}:\text{Cl}$.

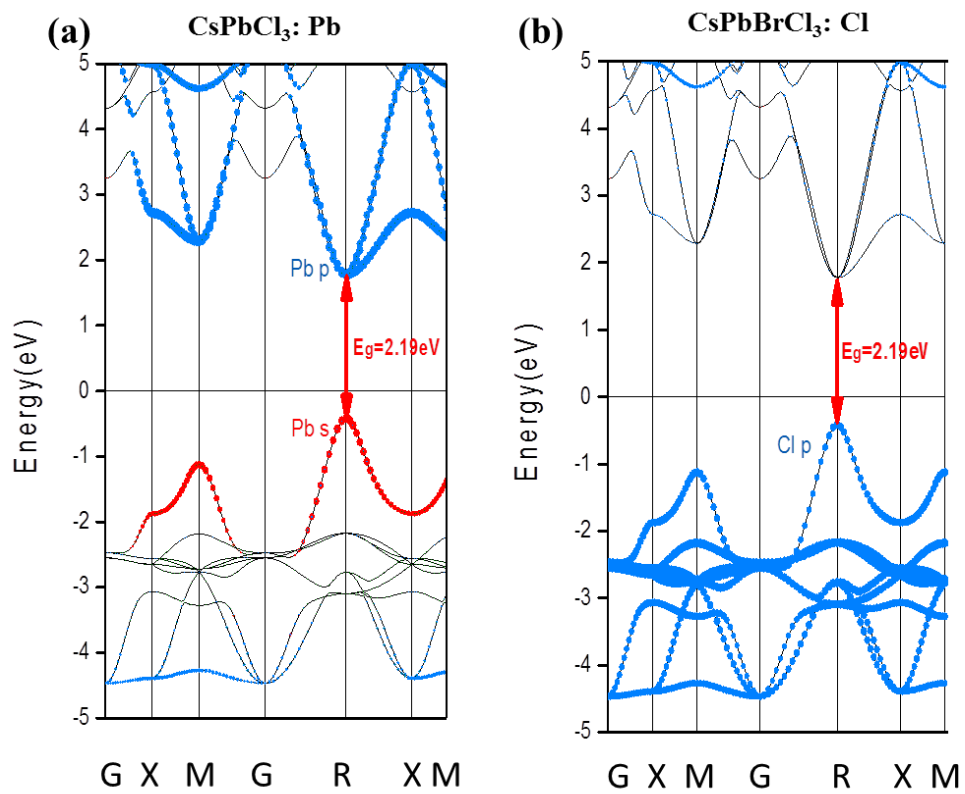


Figure S11. GGA projective band of (a) CsPbCl₃:Pb and (b) CsPbCl₃:Cl.

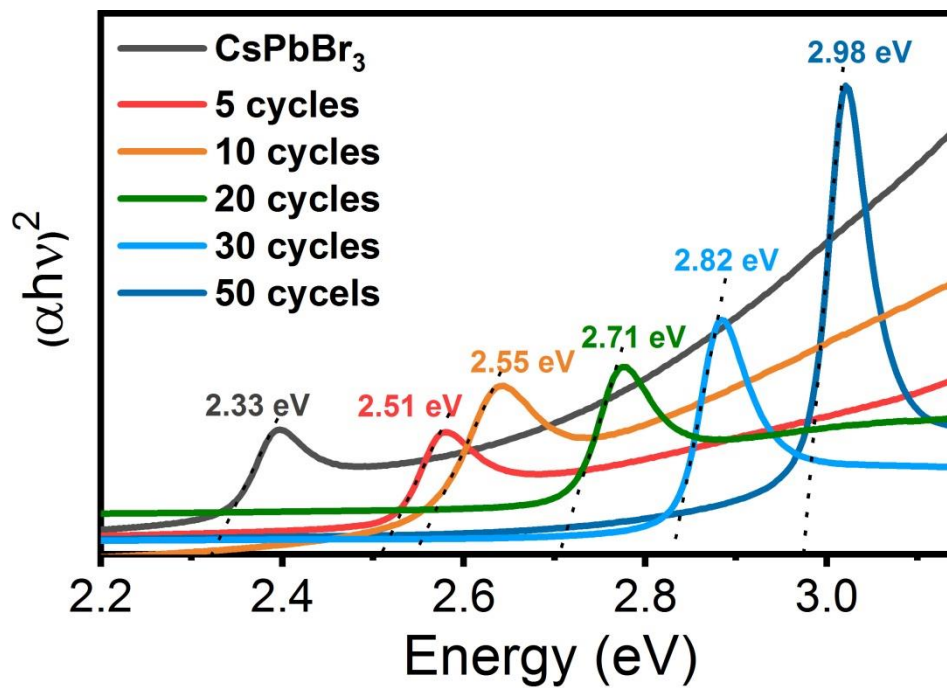


Figure S12. Band gaps of perovskites under different gas injection cycles.

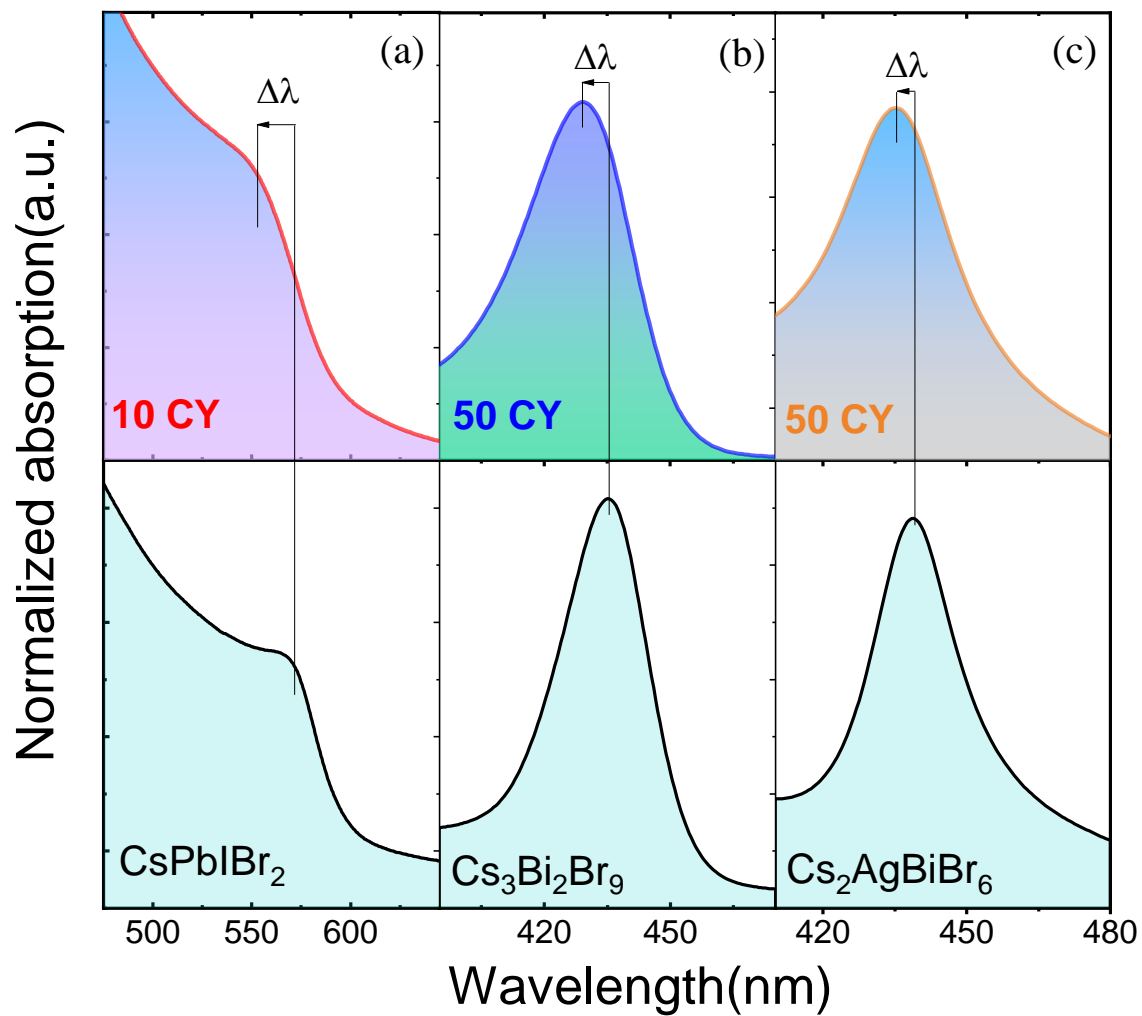


Figure S13. General strategy for other inorganic perovskites thin films. (a) CsPbIBr₃ film, (b) Cs₃Bi₂Br₉ film and (c) Cs₂AgBiBr₆ film.

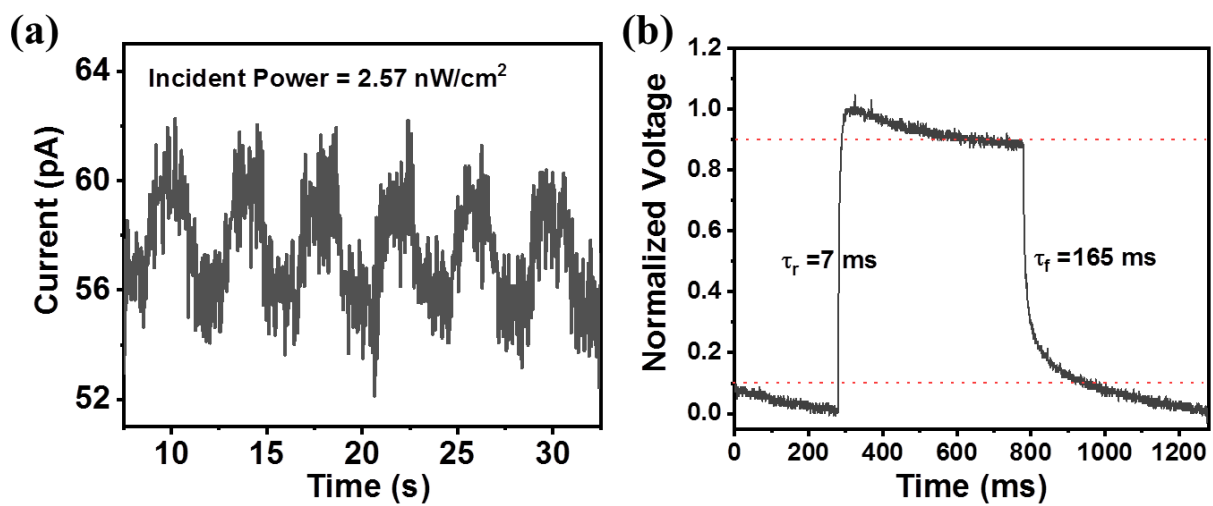


Figure S14. The detection limit (a) and photoresponse speed (b) of CsPbCl₃ UV PDs.

Table S1. Comparison of the bandgaps of CsPbX₃ with previous report. Different methods but the same trends. [1]

Method	CsPbBr ₃	CsPbBr _{1.5} Cl _{1.5}	CsPbCl ₃
GGA	1.7664eV [1.764eV]	1.9808eV	2.1932eV [2.172eV]
GGA+SOC	0.4380eV	0.6515eV	0.8578eV
PBE0	3.0919eV	3.2941eV	3.4671eV
PBE0+SOC	1.2742eV	1.4814eV	1.7552eV
HSE03	2.2809eV	2.5339eV	2.6710eV
HSE06	2.4606eV	2.7227eV	2.8417eV

[1] Ahmad M, Rehman G, Ali L, Shafiq M, Iqbal R, Ahmad R, *et al.* Structural, electronic and optical properties of CsPbX₃ (X=Cl, Br, I) for energy storage and hybrid solar cell applications. *Journal of Alloys and Compounds* 2017, **705**: 828-839.